

Spectral and Imaging Observations of a C2.3 White-Light Flare from the *Advanced Space-Based Solar Observatory* (ASO-S) and the *Chinese H α Solar Explorer* (CHASE)

Qiao Li^{1,2} · Ying Li^{1,2} · Yang Su^{1,2} ·
Dechao Song¹ · Hui Li^{1,2} · Li Feng^{1,2} ·
Yu Huang^{1,2} · Youping Li^{1,2} ·
Jingwei Li¹ · Jie Zhao¹ · Lei Lu¹ ·
Beili Ying¹ · Jianchao Xue¹ ·
Ping Zhang¹ · Jun Tian^{1,2} ·
Xiaofeng Liu^{1,2} · Gen Li^{1,2} ·
Zhichen Jing^{1,2} · Shuting Li^{1,2} ·
Guanglu Shi^{1,2} · Zhengyuan Tian^{1,2} ·
Wei Chen^{1,2} · Yingna Su^{1,2} ·
Qingmin Zhang^{1,2} · Dong Li^{1,2} ·
Yunyi Ge¹ · Jiahui Shan^{1,2} · Yue Zhou^{1,2} ·
Shijun Lei¹ · Weiqun Gan^{1,3}

© Springer

Abstract Solar white-light flares are characterized by an enhancement in the optical continuum, which are usually large flares (say X- and M-class flares). Here we report a small C2.3 white-light flare (SOL2022-12-20T04:10) observed by the *Advanced Space-based Solar Observatory* and the *Chinese H α Solar Explorer*. This flare exhibits an increase of $\approx 6.4\%$ in the photospheric Fe I line at 6569.2 Å and $\approx 3.2\%$ in the nearby continuum. The continuum at 3600 Å also shows an enhancement of $\approx 4.7\%$. The white-light brightening kernels are mainly located at the flare ribbons and co-spatial with nonthermal hard X-ray sources, which implies that the enhanced white-light emissions are related

✉ Y. Li
yingli@pmo.ac.cn

- ¹ Key Laboratory of Dark Matter and Space Astronomy, Purple Mountain Observatory, Chinese Academy of Sciences, Nanjing 210023, People's Republic of China
- ² School of Astronomy and Space Science, University of Science and Technology of China, Hefei 230026, People's Republic of China
- ³ University of Chinese Academy of Sciences, Nanjing 211135, China

to nonthermal electron-beam heating. At the brightening kernels, the Fe I line displays an absorption profile that has a good Gaussian shape, with a redshift up to $\approx 1.7 \text{ km s}^{-1}$, while the H α line shows an emission profile though having a central reversal. The H α line profile also shows a red or blue asymmetry caused by plasma flows with a velocity of several to tens of km s^{-1} . It is interesting to find that the H α asymmetry is opposite at the conjugate footpoints. It is also found that the CHASE continuum increase seems to be related to the change of photospheric magnetic field. Our study provides comprehensive characteristics of a small white-light flare that help understand the energy release process of white-light flares.

Keywords: Flares, White-Light, Relation to Magnetic Field, X-Ray Bursts, Spectral Line, Continuum

1. Introduction

Solar white-light flares (WLFs) are identified by a sudden increase in the visible continuum (Neidig and Cliver, 1983; Neidig, 1989). The first WLF (also the first solar flare) was reported by Carrington (1859) and Hodgson (1859). Most WLFs occur in the vicinity of sunspots and manifest as brightening kernels, but some can also occur in a region almost without sunspot (e.g. Hudson et al., 1994) and appear as loop-like structures (e.g. Hudson et al. 1992; Hudson, Wolfson, and Metcalf 2006; Jejčič, Kleint, and Heinzel 2018). While it is generally accepted that WLFs constitute a minority in the overall flare family (Fang et al., 2013) with X- and M-class flares (i.e. major flares) being the most energetic, there are different views suggesting that all flares may exhibit white-light brightenings (e.g. Matthews et al., 2003; Jess et al., 2008; Song et al., 2018). This hypothesis gains support from the discovery of white-light continuum enhancements in small flares.

Up to now, there have been only about 20 C-class WLFs reported including several low C-class ones from both statistical studies (e.g. Matthews et al., 2003; Hudson, Wolfson, and Metcalf, 2006; Song et al., 2018; Song and Tian, 2018; Castellanos Durán and Kleint, 2020) and case analyses (e.g. Jess et al., 2008; Song et al., 2020). Statistically, C-class WLFs exhibit an average increase of $\approx 10\%$ in the visible continuum. Some C-class WLFs with a lower magnitude could display a relatively higher white-light enhancement (e.g. Hudson, Wolfson, and Metcalf, 2006; Song et al., 2018; Song and Tian, 2018), which seems to deviate from the behavior as observed in major flares. Note that this discrepancy may be attributed to sample bias and instrumental limitation. For case studies, Jess et al. (2008) observed a C2.0 WLF showing a white-light kernel with a diameter of $\approx 0.4''$ using the *Swedish Solar Telescope* (SST) among the highest resolution telescopes. This small scale WLF demonstrates an unusually high increase of $\approx 300\%$ in the blue continuum, surpassing a typical enhancement in WLFs. However, degrading the spatial resolution to $1''$ decreases the enhancement to only 1%. In another case study, Song et al. (2020) presented a C2.3 WLF with an enhancement of $\approx 18\%$ observed by the *Helioseismic and Magnetic Imager*

(HMI: Scherrer et al., 2012) on the *Solar Dynamics Observatory* (SDO: Pesnell, Thompson, and Chamberlin, 2012). This particular flare is associated with weak hard X-ray (HXR) emissions, with the white-light enhancement unlikely caused by accelerated electron beams. Its magnetic field morphology and evolution are more supportive of magnetic reconnection in the lower atmosphere (e.g. Ding, Fang, and Yun, 1999; Chen, Fang, and Ding, 2001) rather than in the corona. This suggests that both the non-thermal particle injection and evolution of magnetic fields need to be considered in studying WLFs. Given the scarcity of studies on small WLFs, more attention should be paid to the WLFs with a low magnitude.

Multiple studies have shown a good correlation between the white-light (including the Balmer continuum) and HXR emissions, in terms of both time and space (e.g. Matthews et al. 2003; Metcalf et al. 2003; Hudson, Wolfson, and Metcalf 2006; Wang 2009; Krucker et al. 2011; Martínez Oliveros et al. 2012; Heinzel and Kleint 2014; Heinzel et al. 2017). These results support an electron-beam bombardment (e.g. Hudson, 1972; Aboudarham and Henoux, 1987) plus its subsequent chromospheric condensation (e.g. Gan et al., 1992; Gan and Mauas, 1994; Kowalski et al., 2015) and radiative backwarming (e.g. Machado, Emslie, and Avrett, 1989) processes being related to the white-light brightenings. Some studies further reveal that the footpoint or ribbon with a stronger white-light enhancement shows a stronger HXR flux (e.g. Metcalf et al., 2003; Krucker et al., 2011). However, Chen and Ding (2005) reported a stronger white-light kernel accompanied by a weaker nonthermal energy flux in comparison between two footpoints. Even some cases show no relationship between the white-light and HXR emissions (e.g. Ryan et al., 1983; Ding et al., 1994; Sylwester and Sylwester, 2000; Song et al., 2020). On the other hand, some other heating mechanisms can also play a role in WLFs, such as magnetic reconnection in the lower atmosphere (e.g. Ding, Fang, and Yun, 1999; Chen, Fang, and Ding, 2001), energy dissipation of Alfvén waves (e.g. Emslie and Sturrock, 1982; Fletcher and Hudson, 2008), and soft X-ray (SXR)/ultraviolet (UV) irradiation (e.g. Poland, Milkey, and Thompson, 1988).

Previous studies have indicated that permanent changes in the photospheric magnetic field commonly appear in flares (e.g. Sudol and Harvey, 2005; Castellanos Durán, Kleint, and Calvo-Mozo, 2018). These changes mean that the magnetic components undergo abrupt transformations and do not return to their original levels for a long time. The coronal implosion process (Hudson, 2000) predicts that photospheric fields become more horizontal during flares, thereby changing the line-of-sight (LoS) magnetic field strength [B_{LoS}] (Hudson, Fisher, and Welsch, 2008). This has been used for an interpretation of the appearance of B_{LoS} changes [ΔB_{LoS}] (e.g. Petrie and Sudol, 2010; Gosain, 2012; Sun et al., 2012). However, differences in ΔB_{LoS} between the chromosphere and photosphere suggested that the chromospheric ΔB_{LoS} may not support a contraction of the field line in flare loops (e.g. Kleint, 2017). Recently, a statistical study (Castellanos Durán and Kleint, 2020) showed that white-light brightenings and ΔB_{LoS} in the photosphere can overlap less than 60%, and the areas of these two parameters appear to have a power-law relation. The relationship between ΔB_{LoS} and white-light brightenings deserves a further study, especially for small WLFs.

Spectral analysis is a good way to study the dynamics of plasma in WLFs, especially via some Fe I lines formed in the photosphere (e.g. Babin and Koval, 1992; Lin, Zhang, and Zhang, 1996; Hong et al., 2018). Jurčák et al. (2018) reported a WLF with the response of Fe I lines at 6301.5 Å and 6302.5 Å, which was estimated to originate in the chromosphere instead of photosphere. In addition, the H α line at 6562.8 Å formed from the photosphere to chromosphere can help us understand the physical process of WLFs. This line mainly behaves as an emission profile with a central reversal and a red asymmetry during WLFs (e.g. Babin and Koval, 1992; Zhou, Fang, and Hu, 1997).

In this work, we report a small C2.3 WLF (SOL2022-12-20T04:10) observed by the *Advanced Space-based Solar Observatory* (ASO-S: Gan et al., 2023) and the *Chinese H α Solar Explorer* (CHASE: Li et al., 2022). ASO-S provides images in the white-light continuum at 3600 Å and also HXR spectra at $\approx 10 - 300$ keV. CHASE has spectral observations in the Fe I 6569.2 Å and H α 6562.8 Å lines. All these allow us to study the comprehensive characteristics of this C2.3 WLF when combining with some other multi-wavelength observations. In the following Section 2, we describe the data reduction. Our results are presented in Section 3, followed by a summary and discussion in Section 4.

2. Data Reduction

2.1. Data

The data used in this work are obtained by multiple telescopes. The main telescopes include the *Lyman-alpha Solar Telescope* (LST: Li et al., 2019; Chen et al., 2019; Feng et al., 2019) aboard ASO-S, CHASE, and HMI on SDO. LST consists of three instruments, one of which is the *White-light Solar Telescope* (WST). WST can provide full-disk images in the continuum at 3600 ± 20 Å. The pixel size of the images is $\approx 0.5''$ while the spatial resolution is about $4''$ (Jing et al., 2024). The cadence is two minutes in a routine mode. The level-2.5 (L2.5) data of WST are used here, which have been done for scientific calibration and image registration. CHASE provides spectral data of the Fe I line at 6569.2 Å (6567.8–6570.6 Å) and the H α line at 6562.8 Å (6559.7–6565.9 Å) via a raster scanning mode (RSM). The data have a cadence of ≈ 1 minute, a pixel size of $\approx 1''$, and a spectral resolution of $0.048 \text{ Å pixel}^{-1}$, with a two-binning mode in both space and spectrum. The calibrated L1.5 data are used here (Qiu et al., 2022). The full-disk images of Fe I 6173 Å and the LoS magnetogram presented in the work are obtained from SDO/HMI, which have a pixel size of $0.5''$ and a cadence of 45 seconds.

The *Hard X-ray Imager* (HXI: Zhang et al., 2019; Su et al., 2022) aboard ASO-S is an HXR imaging spectrometer observing the Sun in an energy range of $\approx 10 - 300$ keV with energy and angular resolutions of $\approx 16.5\%$ at 32 keV and $3.1''$, respectively. The HXI L1 data are used in the present study. The *Spectrometer Telescope for Imaging X-rays* (STIX: Krucker et al., 2020) on *Solar Orbiter* (SolO: Müller et al., 2020) has energy and angular resolutions of $\approx 1 \text{ keV @ } 6 \text{ keV}$ and $\geq 7''$, respectively, in a range from 4 keV to 150 keV. Its L1 pixel and

spectrogram data are used here. At the observation time of the flare event, STIX had a separation angle of 19.2° with Earth and a distance of 0.9 AU to the Sun. The *Atmospheric Imaging Assembly* (AIA: Lemen et al., 2012) on SDO provides the images for flare loops in the Extreme ultraviolet (EUV) channel at 131 \AA with a pixel size of $0.6''$ and a cadence of 12 seconds. The SXR 1–8 \AA light curve is from the *X-Ray Sensor* (XRS: Hanser and Sellers, 1996) aboard the *Geostationary Operational Environmental Satellite* (GOES) with a high cadence of 1 second.

2.2. Data Reduction

We make a co-alignment for the images from different instruments via the routines in the SolarSoftWare (SSW: Freeland and Handy 1998). Firstly, the AIA and HMI images are registered using `aia_prep.pro`. The solar rotation has been removed via `drot_map.pro`. Then the white-light images from WST and CHASE are co-aligned with the HMI continuum images using `xyoff.pro` based on cross correlation for sunspot features. The uncertainty of the co-alignment is estimated to be about $1''$.

For HXI light curves at 20–50 keV and 50–100 keV, we use the combined data of three total flux detectors (D92, D93, and D94) with a cadence of four seconds. The images are reconstructed using HXI CLEAN algorithm (Su et al., 2019b) with sub-collimators G3–G10, which correspond to a spatial resolution of $\approx 6.5''$. We also use STIX data to produce the light curves at 4–10 keV and 10–20 keV with a cadence of four seconds and to reconstruct images via the Expectation Maximization (EM) algorithm (Massa et al., 2019). In addition, we make spectral fitting from STIX via a thermal component plus a nonthermal thick target component. Note that the light-travel time at Earth with a correction of 35 s for STIX has been considered.

In order to remove non-flaring contributions and calculate the relative enhancements caused by flare, we subtract a background or base image from flaring images for different wave bands. For HMI and WST images, an average for 30 minutes before the flare onset is adopted as the background. For CHASE images, the last moment at 04:19:48 UT, i.e. around the flare end time, is selected as the background which is relatively quiet during the whole observation of CHASE. Note that this may lead to an underestimation of the CHASE continuum enhancement to some extent. When estimating the uncertainty of relative enhancements for each wave-band emission, we choose a quiet-Sun region with a size of $100'' \times 16''$ ($X = [-799'', -699'']$, $Y = [483'', 499'']$) to calculate its relative intensity fluctuations, i.e. the error bars as plotted in Figures 3a and b. Note that this quiet-Sun region is out of the field of view of the images as shown in Figures 1d–i.

Using the CHASE spectral data, we can measure the Doppler velocities of Fe I and $H\alpha$ lines and also calculate the $H\alpha$ asymmetry. The reference line centers of Fe I and $H\alpha$ are determined by averaging the profiles over the quiet-Sun region as mentioned above. The excess profile, i.e. after subtracting the background profile, is adopted to obtain the Doppler velocity. For Fe I, a single Gaussian fit with a linear background is used and the average of the background is further

used to define the nearby continuum. It is found that the intensity of this defined continuum is approximately equal to that at the wavelength of 6568.6 Å. For H α , bisector (e.g. Chae et al., 2013) and moment analyses are applied to derive its Doppler velocity. The velocity uncertainties of Fe I and H α lines are estimated to be within ± 0.6 and ± 3.9 km s $^{-1}$, respectively. The H α asymmetry is calculated based on its original profiles. Referring to Equation (1) in Asai et al. (2012), the asymmetry is expressed as follows,

$$RA = \frac{I_{rp} - I_{bp}}{I_{rp} + I_{bp}}, \quad (1)$$

where I_{rp} and I_{bp} denote the peaks of H α red and blue wings, respectively. A positive/negative RA represents a red/blue asymmetry. The uncertainty of the asymmetry is estimated to be about ± 0.014 . When showing the profiles of Fe I and H α (in Figures 3c–f and 4a–d), we make a normalization by using the nearby quiet-Sun continuum, i.e. in a contrast way. More specifically, the nearby quiet-Sun continuum intensity of the H α line is determined by averaging the intensities of the ten wavelength points in its bluest wing, while that of the Fe I line is defined as the average of the linear background of this line.

To investigate the relationships of white-light emission with B_{LoS} and ΔB_{LoS} in the photosphere, the magnetograms from HMI are reshaped into the same pixel size as CHASE images. Then a stepwise function (Sudol and Harvey, 2005) describes the temporal evolution of B_{LoS} as expressed by

$$B_{LoS}(t) = a + bt + c \left\{ 1 + \frac{2}{\pi} \tan^{-1}[n(t - t_0)] \right\}, \quad (2)$$

in which t represents time and a , b , c , n , and t_0 are free parameters to fit. From this stepwise function, the characterized start time [$t_s = t_0 - \pi n^{-1}$] and end time [$t_e = t_0 + \pi n^{-1}$] can also be obtained. ΔB_{LoS} is derived mainly via the method in Castellanos Durán, Kleint, and Calvo-Mozo (2018), which could be expressed as:

$$\Delta B_{LoS} = \begin{cases} \frac{sgn(t_{max} - t_{min})[B_{LoS}(t_{max}) - B_{LoS}(t_{min})]}{2c} \\ B_{LoS}(t_e) - B_{LoS}(t_s) - 2\pi bn^{-1} \end{cases}, \quad (3)$$

where t_{max} and t_{min} represent the times of the maximum and minimum of B_{LoS} , respectively, and the function $sgn(x)$ represents the positive or negative sign of x . Here we also modify some criteria as follows.

1. In this short-duration event, the time range of fit is reduced to 60 minutes centered at the GOES peak time.
2. The duration parameter [πn^{-1}] must be smaller than the fit period, otherwise $\Delta B_{LoS} = 0$.
3. t_s must be earlier than t_e , otherwise $\Delta B_{LoS} = 0$.
4. Both t_s and t_e must be within the fit period, otherwise $\Delta B_{LoS} = 0$.

Note that the noise level of B_{LoS} and ΔB_{LoS} is determined as about ten Gauss (Liu et al., 2012).

3. Results

3.1. Overview of the C2.3 Event

The event under study is a GOES C2.3 flare (SOL2022-12-20T04:10) occurring in NOAA active region 13171 (N26E59). This flare began at 03:46 UT, peaked at 04:10 UT, and ended at 04:19 UT on 20 December 2022 (see the GOES SXR 1–8 Å light curve as shown in Figure 1a), showing a relatively long slow rise before 04:04 UT. CHASE observations covered the main period of the flare from 04:04 to 04:20 UT (denoted by two green vertical lines in Figure 1a), which we focus on in the following. Figure 1b plots the HXR light curves at different energy bands from STIX and HXI, together with the SXR 1–8 Å flux and its temporal derivative. We can see that the HXR 10–20 as well as 20–50 keV emissions peak around the same time as the SXR temporal derivative, indicating the Neupert effect (Neupert, 1968). Note that the flare has no response in HXR emission above ≈ 50 keV. Figure 1c shows multiple emission curves integrated over the flaring core region as marked by the green box in Figures 1d–i. It is seen that the emissions at WST 3600 Å and CHASE H α exhibit a notable rise followed by a decay during the flare. Note that their emission peaks may not represent the true peaks due to a low cadence of more than one minute. It is interesting that the CHASE and HMI continuum emissions show a similar trend, though having multiple peaks during the observation period. It should be mentioned that the main peaks of CHASE and HMI emissions appear in the main phase of the flare.

Figures 1d–i display multi-wavelength images of the flaring region around the flare peak time. We find two main white-light brightening kernels, referred to as K1 and K2, from the base-difference images of HMI, CHASE, and WST continua (Figures 1d–f). These two kernels are located near a small pore (indicated by a black arrow) as seen in the HMI and CHASE continuum images in Figures 1d and e. From the HMI magnetogram in Figure 1g, we can see that K1 is located in negative polarities with a relatively strong magnetic field, while K2 seems to lie in a mix of positive and negative polarities with a weak field, which may be influenced by a projection effect. These two kernels are co-spatial with the H α ribbons as shown in Figure 1h. K1 is located in the center of the south ribbon with a bright H α source, while K2 lies on the edge of the north ribbon with a relatively weak H α brightening. From the AIA 131 Å image in Figure 1i, one can see that K1 and K2 connect the same set of flare loops, which are likely to be a pair of conjugate footpoints.

3.2. Spatial Relationship of the White-light Kernels with Nonthermal HXR Sources

Figure 2 shows the HXR spectral imaging and fitting from STIX and HXI for the C2.3 flare. From the spectral fitting (Figure 2e), we can see a nonthermal component above ≈ 20 keV. Thus, we reconstruct the HXR images at 20–35 keV from HXI for the main nonthermal sources. In addition, we reconstruct the HXR images at 16–28 keV and 4–10 keV from STIX for nonthermal and also thermal sources. These HXR sources corresponding to the flare ribbons and also

loops are overplotted on AIA 131 Å, WST 3600 Å, and CHASE continuum and H α images (Figures 2a–d). At an earlier time of 04:09:22 UT (Figures 2a and b), the nonthermal HXR sources at 20–35 keV are mainly cospatial with the flare ribbons. In particular, the two white-light kernels, K1 and K2, match the nonthermal sources well. It is noted that K1 is close to the nonthermal source with a larger HXR flux while K2 corresponds to the one with a lower flux. At a later time of 04:09:38 UT (Figures 2c and d), the HXR sources evolve a little while K1 is still close to one of the nonthermal HXR sources. These results suggest that the white-light emissions are related to a nonthermal electron-beam heating although the timings of white-light emissions and HXR sources are not conclusive due to a low cadence of the white-light data from WST and CHASE.

3.3. Spectral Features of the White-light Kernels

Figures 3a and b show the temporal evolution of the relative enhancements of continuum and spectral line emissions from HMI, WST, and CHASE, which are integrated over an area of $3'' \times 3''$ for the two white-light kernels K1 and K2. One can see that at K1 (Figure 3a), all the enhancement curves exhibit an evident rise and then a decay during the flare. The maximum enhancements or increases of HMI, CHASE, and WST continua at $\approx 04:10$ UT are 3.9%, 3.2%, and 4.7%, respectively. For comparison, the CHASE Fe I line core and integrated H α line over ± 2.3 Å have larger maximum increases of 6.4% and 38.0%, respectively. At K2 (Figure 3b), the maximum increases of HMI, CHASE, and WST continua, as well as CHASE Fe I core and H α line for their main peaks at $\approx 04:10$ UT are 4.3%, 3.0%, 1.9%, 2.2%, and 20.2%, respectively, most of which are smaller than the corresponding values at K1. Note that the other peaks in the HMI and CHASE continua, say, before 04:08 UT and after 04:15 UT, might be unrelated to the flare itself, as no obvious response is found in the HXR emissions.

Figures 3c–f exhibit the temporal evolution of CHASE Fe I and H α line profiles averaged over an area of $3'' \times 3''$ at K1 and K2. One can see that at both kernels, the Fe I line remains an absorption profile with a symmetric Gaussian shape during the flare (Figures 3c–d). Its line core as well as the nearby continuum have an increase followed by a decrease in the intensity over time. The H α line varies from an absorption to an emission and then back to an absorption profile (Figures 3e–f). Its emission profiles display a central reversal with double peaks in line wings, which are not symmetric. K1 shows a red asymmetry but K2 has a blue asymmetry, namely the conjugate footpoints have an opposite asymmetry in H α .

We further select the Fe I and H α line profiles with maximum intensities at 04:10:19 UT to derive the Doppler velocity as shown in Figures 4a–d. Note that the excess profiles are adopted to do a Gaussian fit for Fe I and to make a moment plus a bisector analysis for H α . One can see that the Fe I line at K1 exhibits a trivial redshift velocity which is actually within the uncertainty (Figure 4a). By contrast, the excess Fe I emission at K2 has an evident redshift with a velocity of 1.70 km s^{-1} (Figure 4b), indicative of a plasma downflow at the lower atmospheric layer. The excess H α profiles with a red or blue asymmetry at K1 and K2 show a much larger redshift or blueshift velocity (Figures 4c–d).

At K1, the measured Doppler velocity is 14.67/20.81 km s⁻¹ (i.e. redshift) from a moment/bisector method. Meanwhile at K2, the velocity is -3.35/-3.59 km s⁻¹ (blueshift) via moment/bisector. Note that the velocity from the bisector is a median of the ones obtained at different intensity levels.

Moreover, we derive the H α Doppler velocity map via moment for the time at 04:10:19 UT as shown in Figure 4e. To get a reliable result, we artificially set the velocity to 0 when the peak intensity of the excess profile in a pixel is less than 100 DN. It is seen that evident Doppler velocities mainly come from the two brightened flare ribbons as marked by green contours (same as the white contours in Figure 1h), whose excess intensities are larger than 500 DN. In particular, H α can show redshift and blueshift velocities at the conjugate footpoints, which has been revealed from the profiles at K1 and K2 as described above. We also plot the asymmetry map in Figure 4f. One can see that only at the flare ribbons, the H α profiles show a notable red or blue asymmetry with an obvious line-wing enhancement. Note that the asymmetry distribution looks quite similar to that of Doppler velocity at the two ribbons, which can also be revealed by the scatter plot in Figure 6i. However, one should caution that the red (blue) asymmetry of H α profiles, or the measured redshift (blueshift) velocity is not necessarily caused by a plasma downflow (upflow), as already revealed in previous studies (e.g. Gan, Rieger, and Fang, 1993; Heinzel et al., 1994; Ding and Fang, 1996; Kuridze et al., 2015). It is also interesting to see that the asymmetry is reversed for the conjugate footpoints at K1 and K2. As given in Figures 4c and d, the asymmetries of H α profiles at K1 and K2 are 0.079 and -0.036, respectively.

3.4. Photospheric Magnetic Field Changes at the White-light Kernels

Figure 5a shows the map of photospheric magnetic field change, i.e., ΔB_{LoS} , for the flare region. We can see some notable changes in B_{LoS} (high ΔB_{LoS}) near/at the white-light kernels K1 and K2. Note that some prominent changes of B_{LoS} also appear in some other regions without white-light brightenings, which is actually similar to the study of Castellanos Durán and Kleint (2020). We further plot the temporal evolution of B_{LoS} at K1 and K2 as well as the fit using a stepwise function in Figures 5b and c. It is seen that there seems to be no obvious change in B_{LoS} , i.e. with a poor fit, at K1, while at K2, there exists an evident change in B_{LoS} with a value of 40.5 Gauss during the flare. In fact, the relationship between the white-light emission and B_{LoS} in this small WLF is somewhat similar to the results in Castellanos Durán and Kleint (2020).

3.5. Statistical Relationships among Different Parameters from Flare Ribbons

We check the statistical relationships among different parameters within the two flare ribbons (marked by the contours in Figures 1h, 4e and f, and 5a). To increase the reliability, here we collect all the available time frames in observations, namely four frames for the CHASE continuum around its maximum, WST continuum, HMI B_{LoS} , and CHASE H α asymmetry but only one frame for

HMI ΔB_{LoS} . Figures 6a–c show the scatter plots of CHASE continuum increase versus photospheric B_{LoS} , ΔB_{LoS} , and H α asymmetry. Note that the data points in the shaped area, i.e. within uncertainties, are excluded to further calculate the linear Pearson correlation coefficient (cc). It is seen that the CHASE continuum increase only has some correlation with ΔB_{LoS} (cc=0.52). In contrast, it has no obvious relationship with B_{LoS} (cc=−0.01) or H α asymmetry (cc=0.25). Figures 6d–f demonstrate the scatter plots of WST continuum increase versus B_{LoS} , ΔB_{LoS} , and H α asymmetry. We find that the continuum increase at WST 3600 Å has no linear relationships with B_{LoS} (cc=−0.28), ΔB_{LoS} (−0.23), or H α asymmetry (cc=0.32). Figures 6g–i exhibit the scatter plots of H α Doppler velocity versus B_{LoS} , ΔB_{LoS} , and H α asymmetry. We can see that H α Doppler velocity has good relationships with B_{LoS} (cc=−0.56) as well as H α asymmetry (cc=0.93). By contrast, it has no good correlation with ΔB_{LoS} (cc=−0.36). Note that the negative correlation between H α velocity and B_{LoS} is owing to negative magnetic fields at most ribbon locations. The implications or explanations of these relationships among different parameters will be discussed in the following Section.

4. Summary and Discussions

In this paper, we perform a comprehensive study of a small C2.3 WLF observed by CHASE and ASO-S, combining with the multi-band observations from SDO and SolO. Our main results are summarized as follows.

1. This small flare shows relative enhancements or increases of 4.3%, 3.2%, 4.7%, and 6.4% in the HMI, CHASE, and WST continua and CHASE Fe I line, respectively. The white-light brightening kernels are mainly located near a small pore as well as within the H α flare ribbons.
2. At the white-light kernels, the CHASE Fe I line remains an absorption profile with a symmetric Gaussian shape during the flare. It can show a redshift velocity up to 1.7 km s^{−1}. By contrast, the H α line changes from an absorption to an emission profile, the latter of which has a central reversal with a line-wing enhancement. In addition, the H α emission profile displays a red or blue asymmetry corresponding to a velocity of several to tens of km s^{−1}.
3. Due to a low cadence of HMI, CHASE, and WST observations, the peak times of white-light emissions and their temporal relationship with the HXR emission are inconclusive in this flare. However, the white-light kernels are found to be co-spatial with the nonthermal HXR sources at 20–35 keV. This suggests that the white-light emissions are related to a nonthermal electron-beam heating, whose radiative backwarming effect could not be excluded.
4. One of the identified white-light kernels is accompanied by a change of photospheric magnetic field [ΔB_{LoS}], while the other is not. Only the CHASE continuum increase at the flare ribbons has a good relationship with ΔB_{LoS} . These confirm that the continuum emission can be linked to ΔB_{LoS} but in an unknown way (Castellanos Durán and Kleint, 2020).
5. The H α Doppler velocity at the flare ribbons has good correlations with B_{LoS} as well as H α asymmetry in this small WLF.

From a statistical perspective (Section 3.5), we find a good correlation between the CHASE continuum increase and photospheric ΔB_{LoS} at flare ribbons, while the case is not between the WST continuum increase at 3600 Å and ΔB_{LoS} . This may be explained by the different formation heights of these two continua. The CHASE continuum near the Fe I line at 6569.2 Å can be formed lower (say in either the photosphere or chromosphere: e.g. Kleint et al. 2016; Kerr 2017) than the WST 3600 Å continuum (i.e. Balmer continuum), the latter of which mainly originates from the chromosphere during a flare (e.g. Avrett, Machado, and Kurucz, 1986). As regards the H α line, it is formed from the photosphere to chromosphere from its wing to core. In particular, this line is sensitive to nonthermal heating (e.g. Henoux, Fang, and Gan 1993; Rubio da Costa et al. 2016; Capparelli et al. 2017). Therefore, its Doppler velocity could reflect chromospheric condensation and probably also evaporation (e.g. Song et al., 2023) caused by nonthermal electron beams. The H α velocity shows some correlation with the photospheric B_{LoS} . This implies that the chromospheric condensation/evaporation can be influenced by the magnetic field in the lower atmosphere particularly in WLFs, as in a WLF, the position of chromospheric condensation/evaporation could be relatively lower in height due to a lower energy deposition height compared with non-WLFs.

This small C2.3 WLF has some properties similar to those of large or major WLFs. (1) The CHASE Fe I and H α lines at the white-light kernels in this small WLF display similar profiles, i.e. symmetric Gaussian profiles still in absorption in Fe I and asymmetric emission profiles with a central reversal in H α , to those in an X1.0 WLF as reported by Song et al. (2023), although their relative increases in the intensity are much lower compared with the X1.0 WLF. (2) The white-light emissions in this small WLF are related to a nonthermal electron-beam heating, which is the same as the case in many large WLFs (e.g. Kuhar et al., 2016; Lee et al., 2017; Song et al., 2023). (3) Some white-light brightening points in this small WLF are accompanied by a photospheric ΔB_{LoS} while some are not. This is consistent with the results in X- and M-class flares (Castellanos Durán and Kleint, 2020). All these may hint that the small WLFs with C and even B class may be the same as the large WLFs with M and X class in nature.

More small WLFs are worthy of study in the future, especially with comprehensive observations. Firstly, combining with HMI continuum images at Fe I 6173 Å (in the Paschen continuum) and WST images at 3600 Å (in the Balmer continuum), we can investigate the types of WLFs, i.e. type I or II with or without a Balmer jump (e.g. Fang and Ding, 1995), as well as the origins of these continuum emissions in small WLFs. In particular, WST provides 3600 Å images with a very high cadence of one second in a burst mode, which can capture some rapid variations of white-light brightenings during a WLF. Secondly, using the spectroscopic observations of Fe I and H α lines from CHASE, we can obtain the dynamics from the photosphere to chromosphere induced by the energy deposition of a WLF. The Doppler velocity and also line width from conjugate footpoints deserve a further study, which could provide some insights into the heating or energy deposition of a WLF. Thirdly, HXR spectral and imaging observations from HXI and/or STIX are necessary to determine the heating mechanisms of a WLF. Some quantitative relationships between

the HXR flux (or even low-energy cutoff or spectral index of the spectrum) and continuum increase further help to establish a detailed relation between the electron-beam heating and white-light emissions in observations. Finally, magnetic field observations from HMI and also the *Full-disk vector Magnetograph* (FMG: Su et al., 2019a) on ASO-S are important to understand how the magnetic field influences the white-light emissions, which has been unknown even in large WLFs. Overall, on the one hand, a statistical study for small WLFs is worthwhile to be performed using high-resolution observations. On the other hand, with the aid of sophisticated radiative hydrodynamic simulations, some case studies are required to understand the energy transportation and deposition as well as emission mechanisms for both large and small WLFs.

Acknowledgments We are very grateful to the anonymous reviewer for his/her valuable suggestions on this manuscript. The ASO-S mission is supported by the Strategic Priority Research Program on Space Science, Chinese Academy of Sciences. The CHASE mission is supported by the China National Space Administration. SDO is a mission of NASA's Living With a Star Program. Solar Orbiter is a space mission of international collaboration between ESA and NASA, operated by ESA. The STIX instrument is an international collaboration between Switzerland, Poland, France, Czech Republic, Germany, Austria, Ireland, and Italy. We thank Shihao Rao, Xiaoshuai Zhu, Bing Wang, Zhentong Li, and Ye Qiu for their help in data processing.

Author contributions Q. Li carried out the data analysis and wrote the first manuscript. Y. Li conceived the idea of the work and revised the manuscript. Y. Su provided the HXI data and imaging. D.C. Song provided suggestions on data analysis. W.Q. Gan is PI of ASO-S. H. Li and L. Feng are PI and Co-PI of LST, respectively. Y. Huang, Y.P. Li, J.W. Li, J. Zhao, L. Lu, B.L. Ying, J.C. Xue, P. Zhang, J. Tian, X.F. Liu, G. Li, J.C. Jing, S.T. Li, G.L. Shi, Z.Y. Tian, W. Chen, Y.N. Su, Q.M. Zhang, D. Li, Y.Y. Ge, J.H. Shan, Y. Zhou, and S.J. Lei contributed to the pipeline and release of ASO-S data. All authors reviewed the manuscript.

Funding The authors are supported by the National Natural Science Foundation of China (NSFC) under grants 12233012 and 12273115, the Strategic Priority Research Program of the Chinese Academy of Sciences under grant XDB0560000, the National Key R&D Program of China under grant 2022YFF0503004, and NSFC under grants 11921003 and 12203102.

Data Availability The ASO-S data used in this work are not publicly available, which were observed during the commissioning phase (from 9 October 2022 to 31 March 2023). However, they are available from the corresponding author on reasonable request. The ASO-S data since 1 April 2023 are publicly available and can be accessed from the official website of ASO-S at aso-s.pmo.ac.cn/sodc/dataArchive.jsp. SDO data are publicly accessible at jsoc.stanford.edu. STIX data are publicly available at datacenter.stix.i4ds.net.

Declarations

Conflict of interest The authors declare no conflicts of interest

References

- Aboudarham, J., Henoux, J.C.: 1987, Non-thermal excitation and ionization of hydrogen in solar flares. II - Effects on the temperature minimum region Energy balance and white light flares. *Astron. Astrophys.* **174**, 270. [ADS](#).

- Asai, A., Ichimoto, K., Kita, R., Kurokawa, H., Shibata, K.: 2012, A Study on Red Asymmetry of $H\alpha$ Flare Ribbons Using a Narrowband Filtergram in the 2001 April 10 Solar Flare. *Pub. Astron. Soc. Japan* **64**, 20. DOI ADS.
- Avrett, E.H., Machado, M.E., Kurucz, R.L.: 1986, Chromospheric flare models. In: Neidig, D.F., Machado, M.E. (eds.) *The Lower Atmosphere of Solar Flares*, 216. ADS.
- Babin, A.N., Koval, A.N.: 1992, Spectral observations of the white-light solar flare of June 15, 1991. *Sov. Astron. Lett.* **18**, 294. ADS.
- Capparelli, V., Zuccarello, F., Romano, P., Simões, P.J.A., Fletcher, L., Kuridze, D., Mathioudakis, M., Keys, P.H., Cauzzi, G., Carlsson, M.: 2017, $H\alpha$ and $H\beta$ Emission in a C3.3 Solar Flare: Comparison between Observations and Simulations. *Astrophys. J.* **850**, 36. DOI ADS.
- Carrington, R.C.: 1859, Description of a Singular Appearance seen in the Sun on September 1, 1859. *Mon. Not. Roy. Astron. Soc.* **20**, 13. DOI ADS.
- Castellanos Durán, J.S., Kleint, L.: 2020, The Statistical Relationship between White-light Emission and Photospheric Magnetic Field Changes in Flares. *Astrophys. J.* **904**, 96. DOI ADS.
- Castellanos Durán, J.S., Kleint, L., Calvo-Mozo, B.: 2018, A Statistical Study of Photospheric Magnetic Field Changes During 75 Solar Flares. *Astrophys. J.* **852**, 25. DOI ADS.
- Chae, J., Park, H.-M., Ahn, K., Yang, H., Park, Y.-D., Cho, K.-S., Cao, W.: 2013, Doppler Shifts of the $H\alpha$ Line and the Ca II 854.2 nm Line in a Quiet Region of the Sun Observed with the FISS/NST. *Sol. Phys.* **288**, 89. DOI ADS.
- Chen, B., Li, H., Song, K.-F., Guo, Q.-F., Zhang, P.-J., He, L.-P., Dai, S., Wang, X.-D., Wang, H.-F., Liu, C.-L., Zhang, H.-J., Zhang, G., Wang, Y., Liu, S.-J., Zhang, H.-X., Liu, L., Mao, S.-L., Liu, Y., Peng, J.-H., Wang, P., Sun, L., Liu, Y., Han, Z.-W., Wang, Y.-L., Wu, K., Ding, G.-X., Zhou, P., Zheng, X., Xia, M.-Y., Wu, Q.-W., Xie, J.-J., Chen, Y., Song, S.-M., Wang, H., Zhu, B., Chu, C.-B., Yang, W.-G., Feng, L., Huang, Y., Gan, W.-Q., Li, Y., Li, J.-W., Lu, L., Xue, J.-C., Ying, B.-L., Sun, M.-Z., Zhu, C., Bao, W.-M., Deng, L., Yin, Z.-S.: 2019, The Lyman-alpha Solar Telescope (LST) for the ASO-S mission - II. design of LST. *Res. Astron. Astrophys.* **19**, 159. DOI ADS.
- Chen, P.-F., Fang, C., Ding, M.-D.D.: 2001, Ellerman Bombs, Type II White-light Flares and Magnetic Reconnection in the Solar Lower Atmosphere. *Chin. J. Astron. Astrophys.* **1**, 176. DOI ADS.
- Chen, Q.R., Ding, M.D.: 2005, On the Relationship between the Continuum Enhancement and Hard X-Ray Emission in a White-Light Flare. *Astrophys. J.* **618**, 537. DOI ADS.
- Ding, M.D., Fang, C.: 1996, On a Possible Explanation of Chromospheric Line Asymmetries of Solar Flares. *Sol. Phys.* **166**, 437. DOI ADS.
- Ding, M.D., Fang, C., Yun, H.S.: 1999, Heating in the Lower Atmosphere and the Continuum Emission of Solar White-Light Flares. *Astrophys. J.* **512**, 454. DOI ADS.
- Ding, M.D., Fang, C., Gan, W.Q., Okamoto, T.: 1994, Optical Spectra and Semi-Empirical Model of a White-Light Flare. *Astrophys. J.* **429**, 890. DOI ADS.
- Emslie, A.G., Sturrock, P.A.: 1982, Temperature minimum heating in solar flares by resistive dissipation of Alfvén waves. *Sol. Phys.* **80**, 99. DOI ADS.
- Fang, C., Ding, M.D.: 1995, On the spectral characteristics and atmospheric models of two types of white-light flares. *Astron. Astrophys. Suppl.* **110**, 99. ADS.
- Fang, C., Chen, P.-F., Li, Z., Ding, M.-D., Dai, Y., Zhang, X.-Y., Mao, W.-J., Zhang, J.-P., Li, T., Liang, Y.-J., Lu, H.-T.: 2013, A new multi-wavelength solar telescope: Optical and Near-infrared Solar Eruption Tracer (ONSET). *Res. Astron. Astrophys.* **13**, 1509. DOI ADS.
- Feng, L., Li, H., Chen, B., Li, Y., Susino, R., Huang, Y., Lu, L., Ying, B.-L., Li, J.-W., Xue, J.-C., Yang, Y.-T., Hong, J., Li, J.-P., Zhao, J., Gan, W.-Q., Zhang, Y.: 2019, The Lyman-alpha Solar Telescope (LST) for the ASO-S mission - III. data and potential diagnostics. *Res. Astron. Astrophys.* **19**, 162. DOI ADS.
- Fletcher, L., Hudson, H.S.: 2008, Impulsive Phase Flare Energy Transport by Large-Scale Alfvén Waves and the Electron Acceleration Problem. *Astrophys. J.* **675**, 1645. DOI ADS.
- Freeland, S.L., Handy, B.N.: 1998, Data Analysis with the SolarSoft System. *Sol. Phys.* **182**, 497. DOI ADS.
- Gan, W.Q., Mauas, P.J.D.: 1994, Atmospheric Heating in Solar Flares by Chromospheric Condensation. *Astrophys. J.* **430**, 891. DOI ADS.
- Gan, W.Q., Rieger, E., Fang, C.: 1993, Semiempirical Flare Models with Chromospheric Condensation. *Astrophys. J.* **416**, 886. DOI ADS.

- Gan, W.Q., Rieger, E., Zhang, H.Q., Fang, C.: 1992, The Role of Chromospheric Condensations in the Continuum Emission of White-Light Flares. *Astrophys. J.* **397**, 694. DOI ADS.
- Gan, W., Zhu, C., Deng, Y., Zhang, Z., Chen, B., Huang, Y., Deng, L., Wu, H., Zhang, H., Li, H., Su, Y., Su, J., Feng, L., Wu, J., Cui, J., Wang, C., Chang, J., Yin, Z., Xiong, W., Chen, B., Yang, J., Li, F., Lin, J., Hou, J., Bai, X., Chen, D., Zhang, Y., Hu, Y., Liang, Y., Wang, J., Song, K., Guo, Q., He, L., Zhang, G., Wang, P., Bao, H., Cao, C., Bai, Y., Chen, B., He, T., Li, X., Zhang, Y., Liao, X., Jiang, H., Li, Y., Su, Y., Lei, S., Chen, W., Li, Y., Zhao, J., Li, J., Ge, Y., Zou, Z., Hu, T., Su, M., Ji, H., Gu, M., Zheng, Y., Xu, D., Wang, X.: 2023, The Advanced Space-Based Solar Observatory (ASO-S). *Sol. Phys.* **298**, 68. DOI ADS.
- Gosain, S.: 2012, Evidence for Collapsing Fields in the Corona and Photosphere during the 2011 February 15 X2.2 Flare: SDO/AIA and HMI Observations. *Astrophys. J.* **749**, 85. DOI ADS.
- Hanser, F.A., Sellers, F.B.: 1996, Design and calibration of the GOES-8 solar x-ray sensor: the XRS. In: Washwell, E.R. (ed.) *GOES-8 and Beyond, Soc. of Photo-Opt. Instrum. Eng. (SPIE) CS-2812*, 344. DOI ADS.
- Heinzl, P., Kleint, L.: 2014, Hydrogen Balmer Continuum in Solar Flares Detected by the Interface Region Imaging Spectrograph (IRIS). *Astrophys. J. Lett.* **794**, L23. DOI ADS.
- Heinzl, P., Karlicky, M., Kotrc, P., Svestka, Z.: 1994, On the Occurrence of Blue Asymmetry in Chromospheric Flare Spectra. *Sol. Phys.* **152**, 393. DOI ADS.
- Heinzl, P., Kleint, L., Kašparová, J., Krucker, S.: 2017, On the Nature of Off-limb Flare Continuum Sources Detected by SDO/HMI. *Astrophys. J.* **847**, 48. DOI ADS.
- Henoux, J.C., Fang, C., Gan, W.Q.: 1993, Diagnostics of non-thermal processes in chromospheric flares. II. H alpha and CaII K line profiles of an atmosphere bombarded by 100 KeV-1 MeV protons. *Astron. Astrophys.* **274**, 923. ADS.
- Hodgson, R.: 1859, On a curious Appearance seen in the Sun. *Mon. Not. Roy. Astron. Soc.* **20**, 15. DOI ADS.
- Hong, J., Ding, M.D., Li, Y., Carlsson, M.: 2018, Non-LTE Calculations of the Fe I 6173 Å Line in a Flaring Atmosphere. *Astrophys. J. Lett.* **857**, L2. DOI ADS.
- Hudson, H.S.: 1972, Thick-Target Processes and White-Light Flares. *Sol. Phys.* **24**, 414. DOI ADS.
- Hudson, H.S.: 2000, Implosions in Coronal Transients. *Astrophys. J. Lett.* **531**, L75. DOI ADS.
- Hudson, H.S., Fisher, G.H., Welsch, B.T.: 2008, Flare Energy and Magnetic Field Variations. In: Howe, R., Komm, R.W., Balasubramaniam, K.S., Petrie, G.J.D. (eds.) *Subsurface and Atmospheric Influences on Solar Activity, Astronomical Society of the Pacific Conference Series* **383**, 221. ADS.
- Hudson, H.S., Wolfson, C.J., Metcalf, T.R.: 2006, White-Light Flares: A TRACE/RHESSI Overview. *Sol. Phys.* **234**, 79. DOI ADS.
- Hudson, H.S., Acton, L.W., Hirayama, T., Uchida, Y.: 1992, White-Light Flares Observed by YOHKOH. *Pub. Astron. Soc. Japan* **44**, L77. ADS.
- Hudson, H.S., Strong, K.T., Dennis, B.R., Zarro, D., Inda, M., Kosugi, T., Sakao, T.: 1994, Impulsive Behavior in Solar Soft X-Radiation. *Astrophys. J. Lett.* **422**, L25. DOI ADS.
- Jejčić, S., Kleint, L., Heinzl, P.: 2018, High-density Off-limb Flare Loops Observed by SDO. *Astrophys. J.* **867**, 134. DOI ADS.
- Jess, D.B., Mathioudakis, M., Crockett, P.J., Keenan, F.P.: 2008, Do All Flares Have White-Light Emission? *Astrophys. J. Lett.* **688**, L119. DOI ADS.
- Jing, Z., Li, Y., Feng, L., Li, H., Huang, Y., Li, Y., Su, Y., Chen, W., Tian, J., Song, D., Li, J., Xue, J., Zhao, J., Lu, L., Ying, B., Zhang, P., Su, Y., Zhang, Q., Li, D., Ge, Y., Li, S., Li, Q., Li, G., Liu, X., Shi, G., Shan, J., Tian, Z., Zhou, Y., Gan, W.: 2024, A Statistical Study of Solar White-Light Flares Observed by the White-Light Solar Telescope of the Lyman-Alpha Solar Telescope on the Advanced Space-Based Solar Observatory (ASO-S/LST/WST) at 360 nm. *Sol. Phys.* **299**, 11. DOI ADS.
- Jurčák, J., Kašparová, J., Švanda, M., Kleint, L.: 2018, Heating of the solar photosphere during a white-light flare. *Astron. Astrophys.* **620**, A183. DOI ADS.
- Kerr, G.S.: 2017, Observations and modelling of the chromosphere during solar flares. PhD thesis, University of Glasgow, UK. ADS.
- Kleint, L.: 2017, First Detection of Chromospheric Magnetic Field Changes during an X1-Flare. *Astrophys. J.* **834**, 26. DOI ADS.

- Kleint, L., Heinzel, P., Judge, P., Krucker, S.: 2016, Continuum Enhancements in the Ultraviolet, the Visible and the Infrared during the X1 Flare on 2014 March 29. *Astrophys. J.* **816**, 88. DOI. ADS.
- Kowalski, A.F., Hawley, S.L., Carlsson, M., Allred, J.C., Uitenbroek, H., Osten, R.A., Holman, G.: 2015, New Insights into White-Light Flare Emission from Radiative-Hydrodynamic Modeling of a Chromospheric Condensation. *Sol. Phys.* **290**, 3487. DOI. ADS.
- Krucker, S., Hudson, H.S., Jeffrey, N.L.S., Battaglia, M., Kontar, E.P., Benz, A.O., Csillaghy, A., Lin, R.P.: 2011, High-resolution Imaging of Solar Flare Ribbons and Its Implication on the Thick-target Beam Model. *Astrophys. J.* **739**, 96. DOI. ADS.
- Krucker, S., Hurford, G.J., Grimm, O., Kögl, S., Gröbelbauer, H.-P., Etesi, L., Casadei, D., Csillaghy, A., Benz, A.O., Arnold, N.G., Molendini, F., Orleanski, P., Schori, D., Xiao, H., Kuhar, M., Hochmuth, N., Felix, S., Schramka, F., Marcin, S., Kobler, S., Iseli, L., Dreier, M., Wiehl, H.J., Kleint, L., Battaglia, M., Lastufka, E., Sathiapal, H., Lapadula, K., Bednarzik, M., Birrer, G., Stutz, S., Wild, C., Marone, F., Skup, K.R., Cichocki, A., Ber, K., Rutkowski, K., Bujwan, W., Juchnikowski, G., Winkler, M., Darmetko, M., Michalska, M., Seweryn, K., Białek, A., Osica, P., Sylwester, J., Kowalinski, M., Ścisłowski, D., Siarkowski, M., Steślicki, M., Mrozek, T., Podgórski, P., Meuris, A., Limousin, O., Gevin, O., Le Mer, I., Brun, S., Strugarek, A., Vilmer, N., Musset, S., Maksimović, M., Fárnik, F., Kozáček, Z., Kašparová, J., Mann, G., Ōnel, H., Warmuth, A., Rendtel, J., Anderson, J., Bauer, S., Dionies, F., Paschke, J., Plüschke, D., Woche, M., Schuller, F., Veronig, A.M., Dickson, E.C.M., Gallagher, P.T., Maloney, S.A., Bloomfield, D.S., Piana, M., Massone, A.M., Benvenuto, F., Massa, P., Schwartz, R.A., Dennis, B.R., van Beek, H.F., Rodríguez-Pacheco, J., Lin, R.P.: 2020, The Spectrometer/Telescope for Imaging X-rays (STIX). *Astron. Astrophys.* **642**, A15. DOI. ADS.
- Kuhar, M., Krucker, S., Martínez Oliveros, J.C., Battaglia, M., Kleint, L., Casadei, D., Hudson, H.S.: 2016, Correlation of Hard X-Ray and White Light Emission in Solar Flares. *Astrophys. J.* **816**, 6. DOI. ADS.
- Kuridze, D., Mathioudakis, M., Simões, P.J.A., Rouppe van der Voort, L., Carlsson, M., Jafarzadeh, S., Allred, J.C., Kowalski, A.F., Kennedy, M., Fletcher, L., Graham, D., Keenan, F.P.: 2015, H α Line Profile Asymmetries and the Chromospheric Flare Velocity Field. *Astrophys. J.* **813**, 125. DOI. ADS.
- Lee, K.-S., Imada, S., Watanabe, K., Bamba, Y., Brooks, D.H.: 2017, IRIS, Hinode, SDO, and RHESSI Observations of a White Light Flare Produced Directly by Nonthermal Electrons. *Astrophys. J.* **836**, 150. DOI. ADS.
- Lemen, J.R., Title, A.M., Akin, D.J., Boerner, P.F., Chou, C., Drake, J.F., Duncan, D.W., Edwards, C.G., Friedlaender, F.M., Heyman, G.F., Hurlburt, N.E., Katz, N.L., Kushner, G.D., Levay, M., Lindgren, R.W., Mathur, D.P., McFeaters, E.L., Mitchell, S., Rehse, R.A., Schrijver, C.J., Springer, L.A., Stern, R.A., Tarbell, T.D., Wuelser, J.-P., Wolfson, C.J., Yanari, C., Bookbinder, J.A., Cheimets, P.N., Caldwell, D., Deluca, E.E., Gates, R., Golub, L., Park, S., Podgorski, W.A., Bush, R.I., Scherrer, P.H., Gumm, M.A., Smith, P., Auker, G., Jerram, P., Pool, P., Souffi, R., Windt, D.L., Beardsley, S., Clapp, M., Lang, J., Waltham, N.: 2012, The Atmospheric Imaging Assembly (AIA) on the Solar Dynamics Observatory (SDO). *Sol. Phys.* **275**, 17. DOI. ADS.
- Li, C., Fang, C., Li, Z., Ding, M., Chen, P., Qiu, Y., You, W., Yuan, Y., An, M., Tao, H., Li, X., Chen, Z., Liu, Q., Mei, G., Yang, L., Zhang, W., Cheng, W., Chen, J., Chen, C., Gu, Q., Huang, Q., Liu, M., Han, C., Xin, H., Chen, C., Ni, Y., Wang, W., Rao, S., Li, H., Lu, X., Wang, W., Lin, J., Jiang, Y., Meng, L., Zhao, J.: 2022, The Chinese H α Solar Explorer (CHASE) mission: An overview. *Science China Phys. Mech and Astron.* **65**, 289602. DOI. ADS.
- Li, H., Chen, B., Feng, L., Li, Y., Huang, Y., Li, J.-W., Lu, L., Xue, J.-C., Ying, B.-L., Zhao, J., Yang, Y.-T., Gan, W.-Q., Fang, C., Song, K.-F., Wang, H., Guo, Q.-F., He, L.-P., Zhu, B., Zhu, C., Deng, L., Bao, H.-C., Cao, C.-X., Yang, Z.-G.: 2019, The Lyman-alpha Solar Telescope (LST) for the ASO-S mission — I. Scientific objectives and overview. *Res. Astron. Astrophys.* **19**, 158. DOI. ADS.
- Lin, Y., Zhang, H., Zhang, W.: 1996, A solar flare in the Fe I 5324 line on 24 June, 1993. *Sol. Phys.* **168**, 135. DOI. ADS.
- Liu, Y., Hoeksema, J.T., Scherrer, P.H., Schou, J., Couvidat, S., Bush, R.I., Duvall, T.L., Hayashi, K., Sun, X., Zhao, X.: 2012, Comparison of Line-of-Sight Magnetograms Taken by the Solar Dynamics Observatory/Helioseismic and Magnetic Imager and Solar and Heliospheric Observatory/Michelson Doppler Imager. *Sol. Phys.* **279**, 295. DOI. ADS.

- Machado, M.E., Emslie, A.G., Avrett, E.H.: 1989, Radiative Backwarming in White-Light Flares. *Sol. Phys.* **124**, 303. DOI ADS.
- Martínez Oliveros, J.-C., Hudson, H.S., Hurford, G.J., Krucker, S., Lin, R.P., Lindsey, C., Couvidat, S., Schou, J., Thompson, W.T.: 2012, The Height of a White-light Flare and Its Hard X-Ray Sources. *Astrophys. J. Lett.* **753**, L26. DOI ADS.
- Massa, P., Piana, M., Massone, A.M., Benvenuto, F.: 2019, Count-based imaging model for the Spectrometer/Telescope for Imaging X-rays (STIX) in Solar Orbiter. *Astron. Astrophys.* **624**, A130. DOI ADS.
- Matthews, S.A., van Driel-Gesztelyi, L., Hudson, H.S., Nitta, N.V.: 2003, A catalogue of white-light flares observed by Yohkoh. *Astron. Astrophys.* **409**, 1107. DOI ADS.
- Metcalf, T.R., Alexander, D., Hudson, H.S., Longcope, D.W.: 2003, TRACE and Yohkoh Observations of a White-Light Flare. *Astrophys. J.* **595**, 483. DOI ADS.
- Müller, D., St. Cyr, O.C., Zouganelis, I., Gilbert, H.R., Marsden, R., Nieves-Chinchilla, T., Antonucci, E., Auchère, F., Berghmans, D., Horbury, T.S., Howard, R.A., Krucker, S., Maksimovic, M., Owen, C.J., Rochus, P., Rodriguez-Pacheco, J., Romoli, M., Solanki, S.K., Bruno, R., Carlsson, M., Fludra, A., Harra, L., Hassler, D.M., Livi, S., Louarn, P., Peter, H., Schühle, U., Teriaca, L., del Toro Iniesta, J.C., Wimmer-Schweingruber, R.F., Marsch, E., Velli, M., De Groof, A., Walsh, A., Williams, D.: 2020, The Solar Orbiter mission. Science overview. *Astron. Astrophys.* **642**, A1. DOI ADS.
- Neidig, D.F.: 1989, The Importance of Solar White-Light Flares. *Sol. Phys.* **121**, 261. DOI ADS.
- Neidig, D.F., Cliver, E.W.: 1983, The Occurrence Frequency of White Light Flares. *Sol. Phys.* **88**, 275. DOI ADS.
- Neupert, W.M.: 1968, Comparison of Solar X-Ray Line Emission with Microwave Emission during Flares. *Astrophys. J. Lett.* **153**, L59. DOI ADS.
- Pesnell, W.D., Thompson, B.J., Chamberlin, P.C.: 2012, The Solar Dynamics Observatory (SDO). *Sol. Phys.* **275**, 3. DOI ADS.
- Petrie, G.J.D., Sudol, J.J.: 2010, Abrupt Longitudinal Magnetic Field Changes in Flaring Active Regions. *Astrophys. J.* **724**, 1218. DOI ADS.
- Poland, A.I., Milkey, R.W., Thompson, W.T.: 1988, Hydrogen and Helium Excitation by Extreme Ultraviolet Radiation for the Production of White-Light Flares. *Sol. Phys.* **115**, 277. DOI ADS.
- Qiu, Y., Rao, S., Li, C., Fang, C., Ding, M., Li, Z., Ni, Y., Wang, W., Hong, J., Hao, Q., Dai, Y., Chen, P., Wan, X., Xu, Z., You, W., Yuan, Y., Tao, H., Li, X., He, Y., Liu, Q.: 2022, Calibration procedures for the CHASE/HIS science data. *Science China Phys. Mech and Astron.* **65**, 289603. DOI ADS.
- Rubio da Costa, F., Kleint, L., Petrosian, V., Liu, W., Allred, J.C.: 2016, Data-driven Radiative Hydrodynamic Modeling of the 2014 March 29 X1.0 Solar Flare. *Astrophys. J.* **827**, 38. DOI ADS.
- Ryan, J.M., Chupp, E.L., Forrest, D.J., Matz, S.M., Rieger, E., Reppin, C., Kanbach, G., Share, G.H.: 1983, Gamma-ray observational constraints on the origin of the optical continuum emission from the white-light flare of 1980 July 1. *Astrophys. J. Lett.* **272**, L61. DOI ADS.
- Scherrer, P.H., Schou, J., Bush, R.I., Kosovichev, A.G., Bogart, R.S., Hoeksema, J.T., Liu, Y., Duvall, T.L., Zhao, J., Title, A.M., Schrijver, C.J., Tarbell, T.D., Tomczyk, S.: 2012, The Helioseismic and Magnetic Imager (HMI) Investigation for the Solar Dynamics Observatory (SDO). *Sol. Phys.* **275**, 207. DOI ADS.
- Song, D.-C., Tian, J., Li, Y., Ding, M.D., Su, Y., Yu, S., Hong, J., Qiu, Y., Rao, S., Liu, X., Li, Q., Chen, X., Li, C., Fang, C.: 2023, Spectral Observations and Modeling of a Solar White-light Flare Observed by CHASE. *Astrophys. J. Lett.* **952**, L6. DOI ADS.
- Song, Y., Tian, H.: 2018, Investigation of White-light Emission in Circular-ribbon Flares. *Astrophys. J.* **867**, 159. DOI ADS.
- Song, Y.L., Tian, H., Zhang, M., Ding, M.D.: 2018, Observations of white-light flares in NOAA active region 11515: high occurrence rate and relationship with magnetic transients. *Astron. Astrophys.* **613**, A69. DOI ADS.
- Song, Y., Tian, H., Zhu, X., Chen, Y., Zhang, M., Zhang, J.: 2020, A White-light Flare Powered by Magnetic Reconnection in the Lower Solar Atmosphere. *Astrophys. J. Lett.* **893**, L13. DOI ADS.
- Su, J.-T., Bai, X.-Y., Chen, J., Guo, J.-J., Liu, S., Wang, X.-F., Xu, H.-Q., Yang, X., Song, Y.-L., Deng, Y.-Y., Ji, K.-F., Deng, L., Huang, Y., Li, H., Gan, W.-Q.: 2019a, Data reduction and calibration of the FMG onboard ASO-S. *Res. Astron. Astrophys.* **19**, 161. DOI ADS.

- Su, Y., Liu, W., Li, Y.-P., Zhang, Z., Hurford, G.J., Chen, W., Huang, Y., Li, Z.-T., Jiang, X.-K., Wang, H.-X., Xia, F.-X.-Y., Chen, C.-X., Yu, W.-H., Yu, F., Wu, J., Gan, W.-Q.: 2019b, Simulations and software development for the Hard X-ray Imager onboard ASO-S. *Res. Astron. Astrophys.* **19**, 163. [DOI](#). [ADS](#).
- Su, Y., Zhang, Z., Gan, W., Wu, J., Jiang, X.: 2022, The Hard X-ray Imager (HXI) on the Advanced Space-based Solar Observatory (ASO-S). In: *Handbook of X-ray and Gamma-ray Astrophysics*. Edited by Cosimo Bambi and Andrea Santangelo, 88. [DOI](#). [ADS](#).
- Sudol, J.J., Harvey, J.W.: 2005, Longitudinal Magnetic Field Changes Accompanying Solar Flares. *Astrophys. J.* **635**, 647. [DOI](#). [ADS](#).
- Sun, X., Hoeksema, J.T., Liu, Y., Wiegmann, T., Hayashi, K., Chen, Q., Thalmann, J.: 2012, Evolution of Magnetic Field and Energy in a Major Eruptive Active Region Based on SDO/HMI Observation. *Astrophys. J.* **748**, 77. [DOI](#). [ADS](#).
- Sylwester, B., Sylwester, J.: 2000, Evolution of White-Light Flares Observed by YOHKOH. *Sol. Phys.* **194**, 305. [DOI](#). [ADS](#).
- Wang, H.-M.: 2009, Study of white-light flares observed by Hinode. *Res. Astron. Astrophys.* **9**, 127. [DOI](#). [ADS](#).
- Zhang, Z., Chen, D.-Y., Wu, J., Chang, J., Hu, Y.-M., Su, Y., Zhang, Y., Wang, J.-P., Liang, Y.-M., Ma, T., Guo, J.-H., Cai, M.-S., Zhang, Y.-Q., Huang, Y.-Y., Peng, X.-Y., Tang, Z.-B., Zhao, X., Zhou, H.-H., Wang, L.-G., Song, J.-X., Ma, M., Xu, G.-Z., Yang, J.-F., Lu, D., He, Y.-H., Tao, J.-Y., Ma, X.-L., Lv, B.-G., Bai, Y.-P., Cao, C.-X., Huang, Y., Gan, W.-Q.: 2019, Hard X-ray Imager (HXI) onboard the ASO-S mission. *Res. Astron. Astrophys.* **19**, 160. [DOI](#). [ADS](#).
- Zhou, X., Fang, C., Hu, J.: 1997, Analysis of high time resolution spectra of the 1991-10-24 white-light flare. *Chin. Astron. Astrophys.* **21**, 99. [DOI](#). [ADS](#).

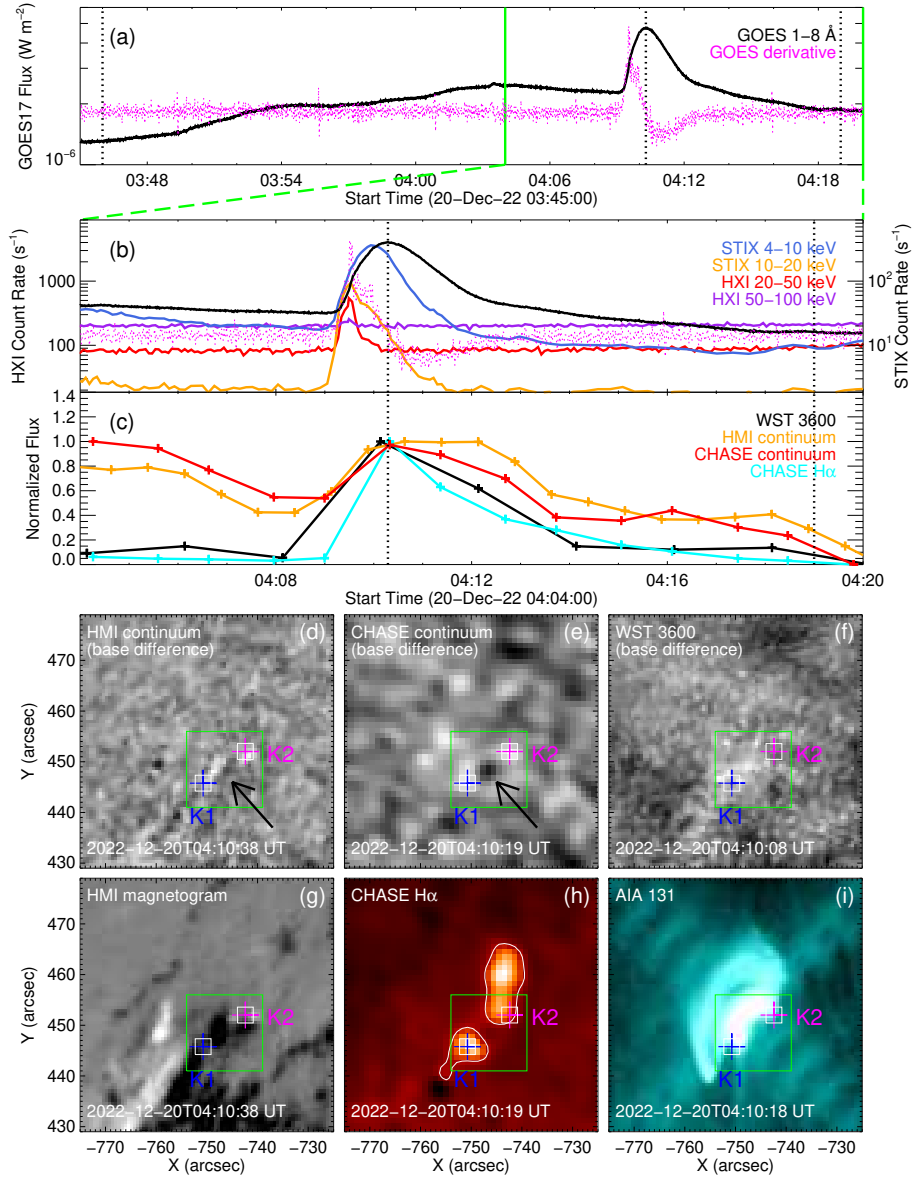


Figure 1. (a) Full-disk GOES SXR 1–8 Å light curve and its temporal derivative for the C2.3 WLF. The *three vertical dotted lines* mark the GOES onset, peak, and end times. The *two green vertical lines* denote the CHASE observation period as shown in Panels b and c. (b) Full-disk light curves of STIX HXR 4–10 keV, STIX HXR 10–20 keV, HXI HXR 20–50 keV, and HXI HXR 50–100 keV, together with GOES SXR 1–8 Å flux and its temporal derivative. (c) Normalized light curves in multiple wavebands from WST, HMI, and CHASE continua and CHASE H α line (summed over ± 2.3 Å). The *two vertical dotted lines* in Panels b and c represent the GOES peak and end times. (d–i) Base-difference images of HMI, CHASE, and WST continua, HMI magnetogram, CHASE H α image, and AIA 131 image near the flare peak time. The *two pluses* in each panel denote the two white-light brightening kernels K1 and K2. The *green box* in Panels d–i marks the flaring region used to make the light curves in Panel c. The *black arrow* in Panels d and e denotes a small pore. The *white contours* in Panel h outline the H α flare ribbons whose excess intensities are larger than 500 DNs.

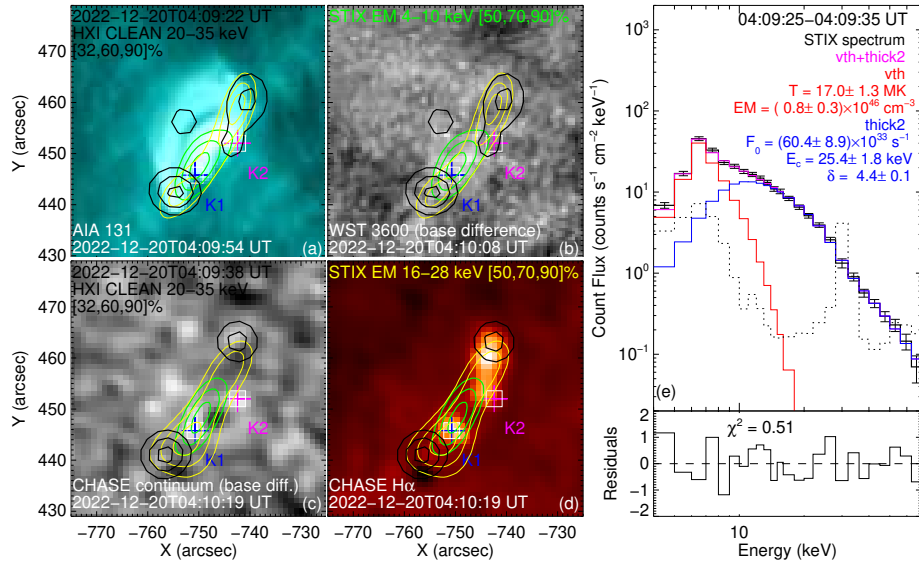


Figure 2. (a–d) HXR imaging from HXI and STIX for two times overlaid on AIA 131 Å, WST 3600 Å, CHASE continuum, and CHASE H α images. The nonthermal and thermal sources are marked by the *black* (HXI 20–35 keV), *yellow* (STIX 16–28 keV), and *green* (STIX 4–10 keV) contours. The *two pluses* in each panel represent the two white-light brightening kernels K1 and K2. (e) STIX HXR background-subtracted count spectrum (*black solid curve*) fitted by an isothermal (*red curve*) plus a nonthermal thick target (*blue curve*) model for the peak time of the HXR 20–50 keV emission. The *gray dashed curve* is the background emission taken during non-flaring times close to the event.

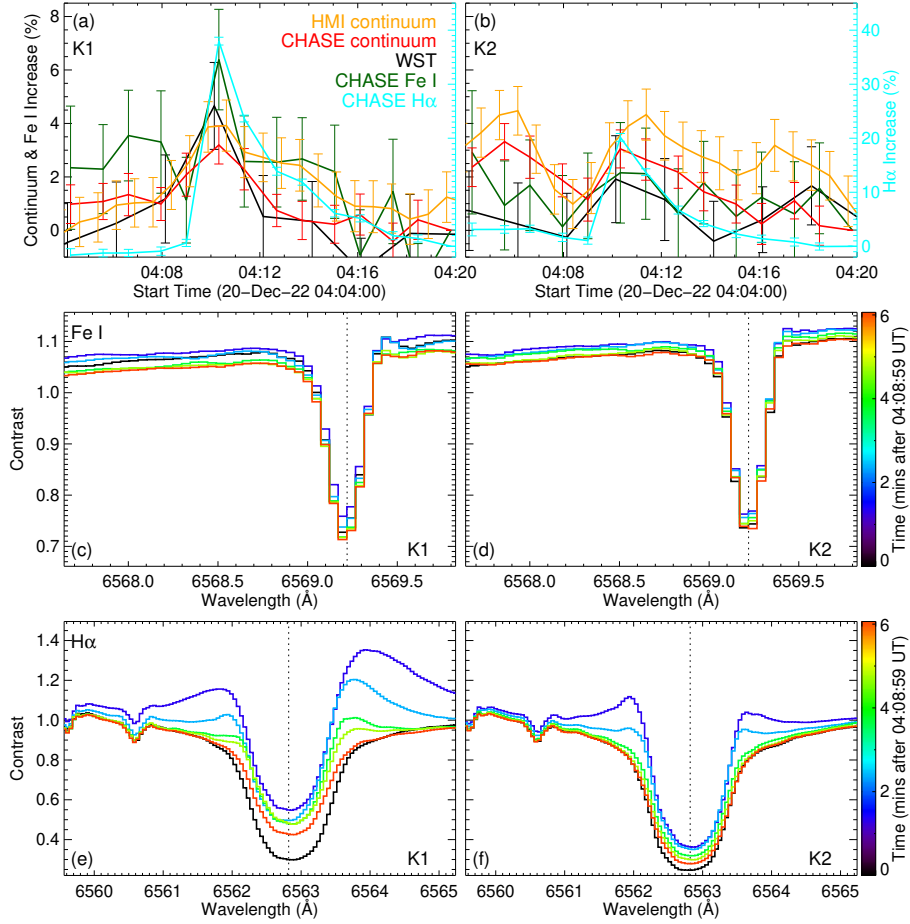


Figure 3. (a) and (b) Temporal evolution of the relative enhancements or increases of HMI continuum, CHASE continuum, WST continuum, Fe I line core, integrated H α line (± 2.3 Å) at the white-light kernels K1 and K2 averaged over an area of $3'' \times 3''$. The *error bars* represent the uncertainties. (c–f) Temporal evolution of the normalized Fe I and H α line profiles at K1 and K2 averaged over an area of $3'' \times 3''$. The *vertical dotted line* in each panel denotes the line center of Fe I or H α .

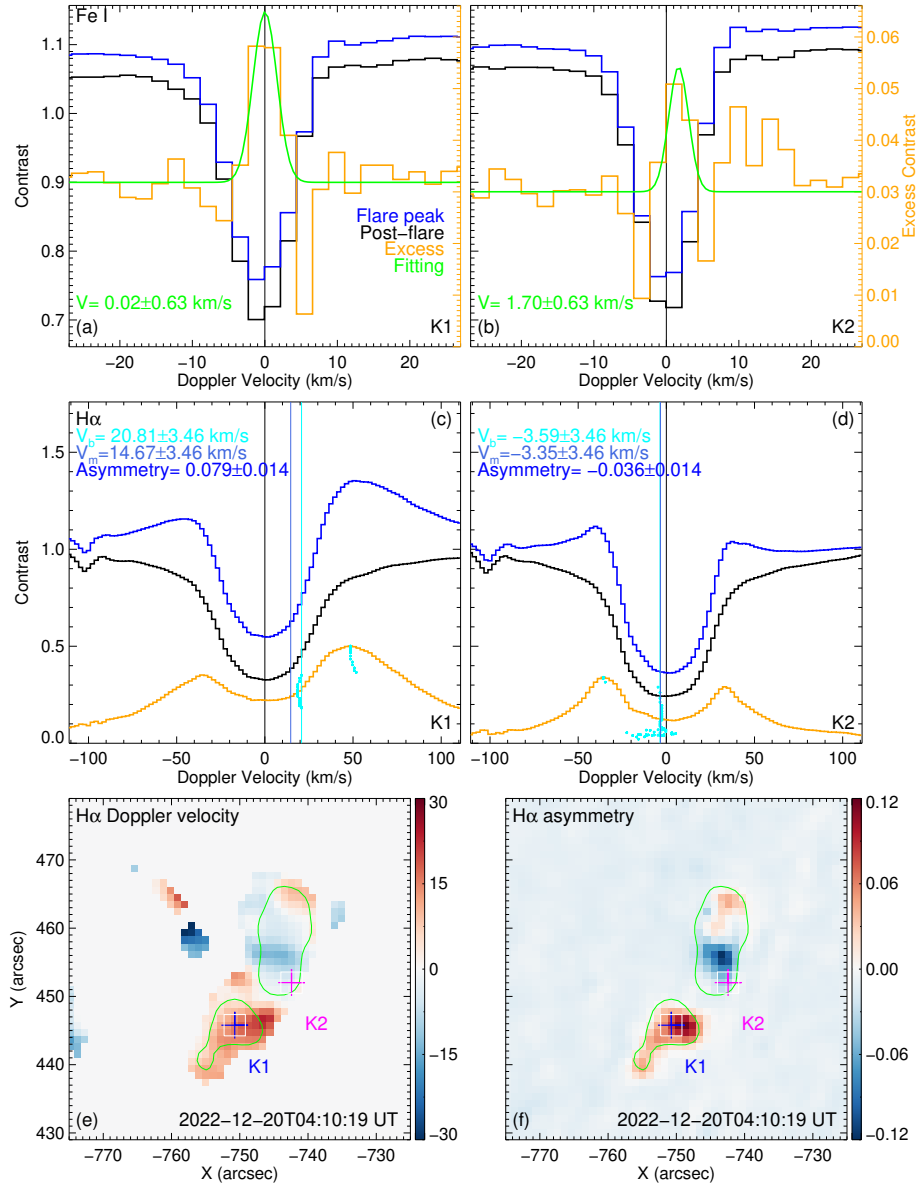


Figure 4. Normalized line profiles of Fe I (a and b) and H α (c and d) from the white-light kernels K1 and K2 averaged over an area of $3'' \times 3''$ at the flare peak time of 04:10:19 UT. The blue, black, and orange curves in each panel indicate the flaring, background, and excess profiles, respectively. The gray vertical line in each panel denotes the line center of Fe I or H α . The green curve in Panels a and b represents a Gaussian fit to the excess Fe I profile. The royal blue and cyan vertical lines in Panels c and d mark the Doppler velocities derived from the moment and bisector methods, respectively, the latter of which is a medium of the velocities obtained at different intensity levels. (e) and (f) Maps of H α Doppler velocity and asymmetry at the flare peak time. The Doppler velocity is calculated by the moment method. The two pluses in each panel represent the two white-light kernels K1 and K2. The green contours denote the H α flare ribbons whose excess intensities are larger than 500 DN.

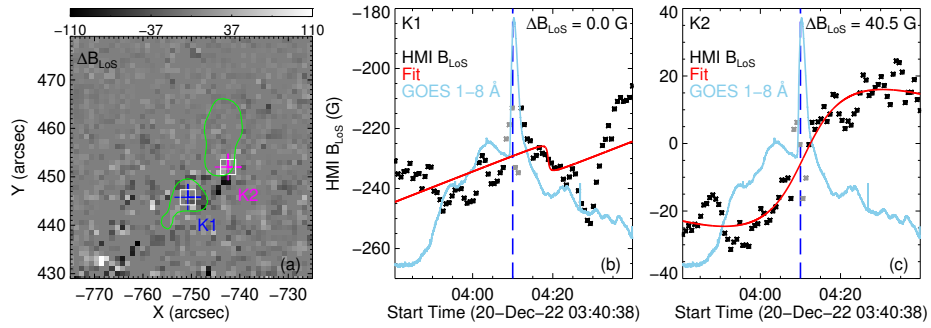


Figure 5. (a) Photospheric ΔB_{LoS} map for the flare active region. The *two pluses* indicate the two white-light kernels K1 and K2 and the *green contours* denote the $\text{H}\alpha$ ribbons whose excess intensities are larger than 500 DNs. (b) and (c) Temporal evolution of HMI B_{LoS} (black dots) at K1 and K2 averaged over an area of $3'' \times 3''$, together with the GOES SXR 1–8 Å light curve (sky blue curve). In each panel, the red line denotes a stepwise function fit to B_{LoS} excluding the five data points (gray dots) around the flare peak time (marked by the blue vertical line).

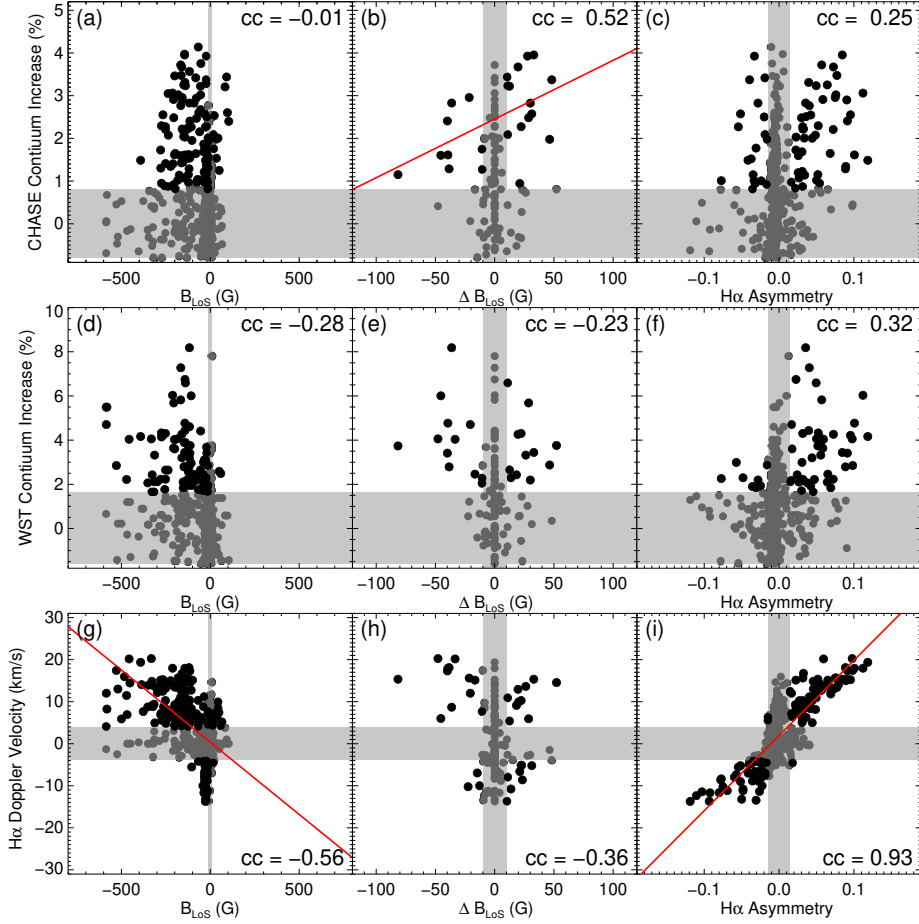


Figure 6. (a–c) Scatter plots of CHASE continuum increase with HMI B_{LoS} , ΔB_{LoS} , and H α asymmetry from flare ribbons. (d–f) scatter plots of WST 3600 Å increase with the above mentioned three parameters. (g–i) Scatter plots of H α Doppler velocity with the three parameters. The *gray area* in each panel denotes the uncertainty of each parameter. We do a linear fit (*red line*) if two parameters among them have a good correlation ($cc \geq 0.5$).